



Semiconducting nanocomposite based on the incorporation of polyaniline on the cellulose extracted from *Bambusa vulgaris*: structural, thermal and electrical properties

Laiane S. da Silva^{1,2} · Matheus M. Biondo^{1,2} · Bianca de A. Feitosa^{1,2} · Ana L. F. Rocha² · Camila da C. Pinto^{1,3} · Suzan X. Lima^{1,2} · Cláudia de L. Nogueira⁴ · Sérgio M. de Souza^{1,3} · Yurimiler L. Ruiz^{1,5} · Pedro H. Campelo^{1,2,3} · Edgar A. Sanches^{1,2}

Received: 18 June 2021 / Accepted: 27 August 2021 / Published online: 13 September 2021
© Institute of Chemistry, Slovak Academy of Sciences 2021

Abstract

Polyaniline Emeraldine-salt (PANI-ES)/Cellulose nanocomposite was synthesized based on the in situ polymerization of aniline over cellulose extracted from *Bambusa vulgaris*. X-ray diffraction (XRD) analysis suggested that the extraction process produced smaller and better oriented cellulose nanocrystals when compared to the bamboo *in-natura* cellulose. PANI-ES influenced on the orientation of the cellulose crystals in the nanocomposite form, increasing the intensity of the planes (0 0 2) and (1 -2 1), besides contributing with more than 60% of the X-ray scattering. Fourier-transform Infrared (FTIR) spectroscopy revealed that characteristic bands of cellulose in the nanocomposite, such as that at 1164 cm^{-1} , presented a red shift about 14 cm^{-1} , probably due to a chemical interaction between matrix and reinforcement. Thermogravimetry/derivative Thermogravimetry (TG/dTG) analysis showed that the nanocomposite degradation in 157 °C was the lowest among the bamboo *in-natura* and extracted cellulose, and it was attributed to the presence of Cl^- counterions in the PANI-ES chains. The dc electrical conductivity values (σ_{dc}) were $8.53 \times 10^{-3}\text{ S/cm}$, $1.05 \times 10^{-4}\text{ S/cm}$ and $2.10 \times 10^{-9}\text{ S/cm}$ for PANI-ES, PANI-ES/Cellulose and extracted cellulose, respectively. Scanning Electron Microscopy (SEM) analysis revealed the formation of a polymer film all over the surface of cellulose fibers.

✉ Matheus M. Biondo
matheusbiondo@ufam.edu.br

¹ Programa de Pós-Graduação em Ciência e Engenharia de Materiais (PPGCEM), Universidade Federal do Amazonas (UFAM), Manaus, AM, Brazil

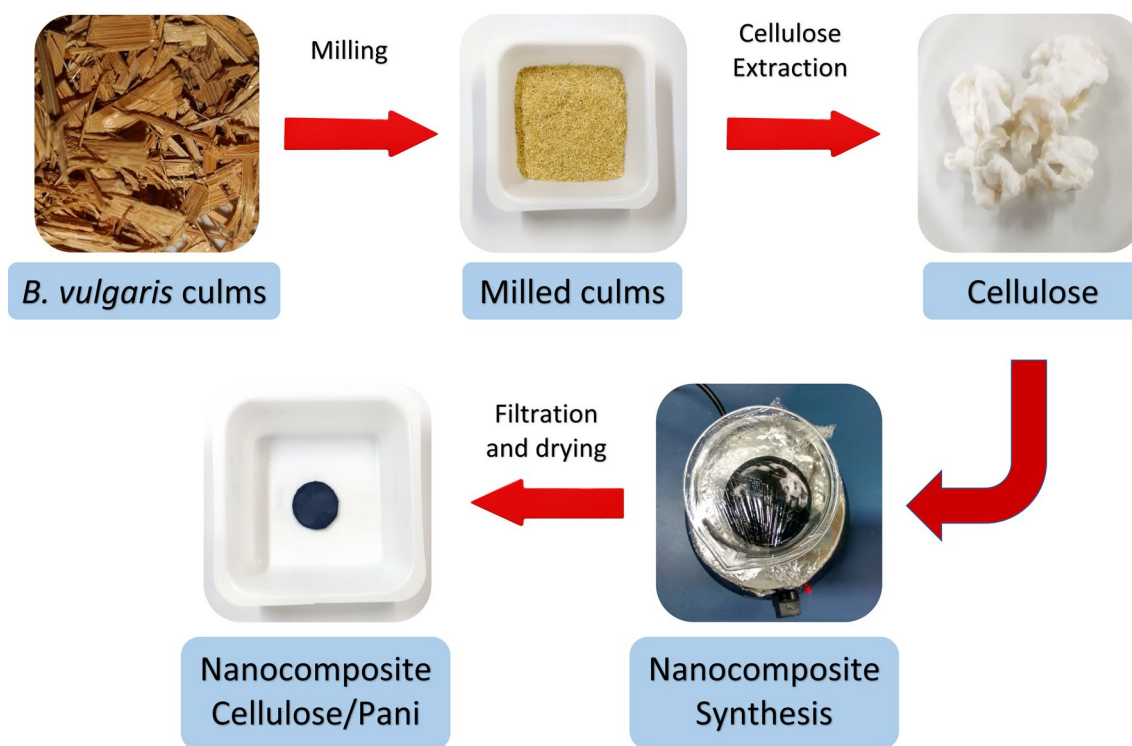
² Laboratório de Polímeros Nanoestruturados (NANOPOL - @nanopol_ufam), Universidade Federal do Amazonas (UFAM), Manaus, AM, Brazil

³ Laboratório de Materiais (LABMat), Universidade Federal do Amazonas (UFAM), Manaus, AM, Brazil

⁴ Escola Superior de Agricultura Luiz de Queiroz – USP/ESALQ, Piracicaba, SP, Brazil

⁵ Laboratório de Processamento de Materiais Tecnológicos (LPMat), Universidade Federal do Amazonas (UFAM), Manaus, AM, Brazil

Graphic abstract



Keywords Polyaniline · *Bambusa vulgaris* · Nanocomposite · Cellulose extraction

Introduction

Cellulose has been considered an alternative material to non-degradable fossil fuel-based polymers due to its abundance and biodegradability (Moon et al. 2011; George and Sabapathi 2015; Yang et al. 2015; He et al. 2019). The chemical structure of cellulose is based on β -1,4-linked glucopyranose units, which bear three hydroxyl groups (Klemm et al. 2005; Zhao et al. 2007; Gurjanov et al. 2008; Mo et al. 2009). Consequently, the hydroxyl groups covering the cellulose backbones (Jie et al. 2019; Svenningsson et al. 2019) as well as the regular arrangement of their macromolecules allow the interaction with a variety of materials (Sharifi et al. 2018; Fei et al. 2019). Bamboos are often called “tree grasses” because of their large branches and woody stems (Xu et al. 2020). As a perennial woody grass, bamboo has become one of the most potential renewable non-woody cellulosic materials because of its high productivity, rapid growth and easy propagation (Visakh et al. 2012; Tanpichai et al. 2019). *Bambusa vulgaris* (L.) (Poaceae) has been extensively found in tropical and subtropical areas (Yakubu and Bukoye 2009) and represents a potential source of cellulose.

Cellulose has been extensively applied in the development of nanocomposites together with conjugated polymers

(Tian et al. 2017; Zhou et al. 2017; Alonso et al. 2018; Hajlaoui et al. 2020) aiming to improve physicochemical and mechanical properties, as well as to propose new technological applications (Palaniappan and Devi 2008; Mo et al. 2009; Luo et al. 2013; Sangamithirai et al. 2015; Zheng et al. 2017; Picanço et al. 2018; Liu et al. 2019; Wang et al. 2019b; Woigk et al. 2019; Cao et al. 2020; Yang et al. 2020; Trindade et al. 2020). However, few studies report a systematic structural approach based on X-ray diffraction analysis (XRD), Rietveld refinement (De Figueiredo and Ferreira 2014; Manzato et al. 2017; Hernandez et al. 2018) and Fourier-transform Infrared spectroscopy (FTIR) focusing on the interaction between both phases as a consequence of the *in-situ* polymerization.

In order to report the effect of the *in-situ* polymerization of aniline on the extracted cellulose from *B. vulgaris*, the PANI-ES/Cellulose nanocomposite was characterized by XRD to examine the long-range order achieved as consequence of very short-range interactions. Rietveld refinement was performed to obtain lattice parameters, crystallite size and microstrain. FTIR technique was applied to molecular structural characterization, as well as to verify some possible chemical interaction between PANI-ES and cellulose fibers. TG/dTG were conducted to evaluate the thermal

stability of the bamboo *in-natura*, extracted cellulose and developed nanocomposite. SEM analysis was carried out to confirm the polymerization of aniline over the cellulose fibers, as well as to evaluate the resulting morphology. Then, these results were correlated with the electrical conductivity data obtained by Complex Impedance Spectroscopy (CIS) analysis.

Experimental

Materials

Chemicals

Aniline, sodium chlorite and ammonium persulfate (APS) were purchased from Sigma-Aldrich®, São Paulo, Brazil. Sodium hydroxide (NaOH), hydrochloric acid (HCl) 37%, glacial acetic acid and acetone were purchased from Synth®, Diadema, Brazil. Reverse osmosis water was used in the whole process.

Plant material

Bambusa vulgaris culms (SisGen n° A26CD5E) were collected in Manaus/AM – Brazil and dried under controlled humidity (50% R.H.) at 27 °C. Botanical identification was carried out at the Federal University of Amazonas (UFAM) following the established protocol.

Methods

Cellulose extraction

B. vulgaris culms were cut into pieces (about 10 cm) and washed using distilled water under constant stirring at (70 ± 2) °C for 60 min. Pieces were dried and then subjected to a knife mill (MA1340, Marconi). The specific chemical treatments employed for cellulose extraction was performed in the following order: extractives, alkalization and bleaching. For removing the extractives, the milled culms were subjected to a solvent mixture of ethanol/acetone (95:5, v/v) for 20 min at (70 ± 2) °C. The system was filtered using a 14 µm pore size filter paper, after reach room temperature. The fibers were washed using distilled water and dried in oven for 4 h at (60 ± 2) °C.

Alkalization treatment was applied to swell raw fibers. Then, fibers were treated with 4 wt% NaOH solution for 1 h at (60 ± 2) °C to reduce hemicellulose and lignin contents. Lignocellulosic fibers resulting from this chemical treatment were washed using distilled water until reach pH 7 and dried to constant weight at 100 °C in oven.

Bleaching treatment was performed to extract cellulose fibers. A solution was prepared using distilled water (360 mL), glacial acetic acid (3 mL) and sodium chlorite (7.5 g). Then, 9.00 g of dry lignocellulosic fibers were added to this solution under constant stirring for 1 h at (70 ± 2) °C. Three additions of the previous amount of glacial acetic acid and sodium chlorite were added to the system at constant stirring in intervals of 1 h. The system was allowed to reach the room temperature, filtered, and washed using distilled water until reach pH 7 for the obtainment of the bleached fibers. These fibers were dried at room temperature and a mass of 7.00 g was obtained.

Nanocomposite preparation

Two different solutions were prepared for the nanocomposite preparation: in Solution I, the dry cellulose extracted previously (3.00 g) was added to 0.72 g of hydrochloride aniline powder monomer in HCl (60 mL, 0.1 mol/L). On the other hand, Solution II was obtained by adding 1.14 g of ammonium persulfate (APS) in HCl (20 mL, 0.1 mol/L). Then, Solution II was added drop-by-drop to Solution I at room temperature. The system remained under constant stirring for 3 h allowing the *in-situ* polymerization of aniline over cellulose surface. The PANI-ES/Cellulose nanocomposite was vacuum filtered, washed using distilled water and maintained in a desiccator until reach constant weight of 3.19 g.

X-ray diffraction and Rietveld refinement

X-ray diffraction technique (XRD) was performed on a Panalytical Empyrean diffractometer, $\text{CuK}\alpha$ ($\lambda = 1.54056 \text{ \AA}$), 40 kV and 40 mA, equipped with a Bragg–Brentano HD mirror, 0.02 rad soller slit, 1° ant-scattering slit and 1/4° divergence slit in the incident beam. The X-ray photons were detected with a PIXcel3D-Medipix3, (1 × 1) area detector. Measurements were performed using a Si single crystal sample-holder from 5° to 100° (2θ), step of 0.01313° and 60 s/step. A LaB_6 standard NIST (660b) was used to account instrumental effects. Rietveld method (Rietveld 1967) implemented in the GSAS software package (Larson and Von Dreele 2004) was used to refine structural parameters and line widths, following the recommendations of IUCr (McCusker et al. 1999).

The peak profile analysis was carried out using the modified Thompson–Cox–Hasting *pseudo*-Voigt profile function (THOMPSON et al. 1987). Chebyshev polynomials were used to fit the background scattering. The relative intensities of the relevant *hkl* reflections was considered by using spherical harmonics preferential orientation model (ODF) (Larson and Von Dreele 2004; Vitalij K. Pecharsky and Zavaliy 2009), allowing the obtainment of the texture index. All

atomic displacements were fixed at 0.025 \AA^2 . The FWHM (Γ) is expressed as follows (Larson and Von Dreele 2004):

$$\Gamma = \sqrt{\Gamma_G^5 + 2.69269\Gamma_G^4\Gamma_L + 2.42843\Gamma_G^3\Gamma_L^2 + 4.47163\Gamma_G^2\Gamma_L^3 + 0.07842\Gamma_G\Gamma_L^4 + \Gamma_L^5} \quad (1)$$

where (Γ_G) and (Γ_L) are Gaussian and Lorentzian parts, respectively:

$$\Gamma_G = \left[(U + (1 - \eta)^2 d_{\text{hkl}}^4 \Gamma_S^2(hkl)) \tan^2 \theta + V \tan \theta + W + \frac{P}{\cos^2 \theta} \right]^{1/2} \quad (2)$$

$$\Gamma_L = \eta d_{\text{hkl}}^2 \Gamma_S(hkl) \tan \theta + \frac{X + X_e \cos \phi}{\cos \theta} \quad (3)$$

The parameter η determines the contributions of the Gaussian ($\eta=0$) and Lorentzian ($\eta=1$) broadening. The refinements were achieved with $\eta=0.75$. In the Gaussian part, the parameters V and W are dependent on the instruments. The parameters P and the term $X + X_e \cos \phi$ describe the Gaussian and the Lorentzian contributions to size and broadening, respectively. The parameters P and X correspond to the isotropic crystallite-size broadening, while X_e expresses the anisotropic crystallite-size effects. The term ϕ represents the angle between a reflection vector and its respective broadening axis. The isotropic (U) and the anisotropic [$\Gamma_S(hkl)$] strain parameters express the peak

broadening due to strain in the crystal lattice. $\Gamma_S(hkl)$ is a hkl -dependent line broadening function that depends on the

crystal symmetry (Stephens 1999).

The Lorentzian (β_L) and Gaussian (β_G) integral widths of the diffraction simulated line can be calculated by using both Γ and η parameters, which are obtained directly from the Rietveld analysis:

$$\beta_G = \frac{\Gamma}{2} \sqrt{\frac{\pi(1 - 0.74417\eta - 0.24781\eta^2 - 0.00810\eta^3)}{\ln 2}} \quad (4)$$

and

$$\beta_L = \frac{\pi\Gamma}{2} (0.72928\eta + 0.19289\eta^2 + 0.07783\eta^3) \quad (5)$$

Thus, the mean crystallite size D (\AA) was calculated by using the Scherrer's equation considering only the best fitted peak (1 1 0):

$$D_{(011)} = \frac{0.91\lambda}{\beta_L \cos \theta} \quad (6)$$

The microstrain, on the other hand, was calculated using the formula:

$$\varepsilon_{(011)} = \beta_G / 4 \tan \theta \quad (7)$$

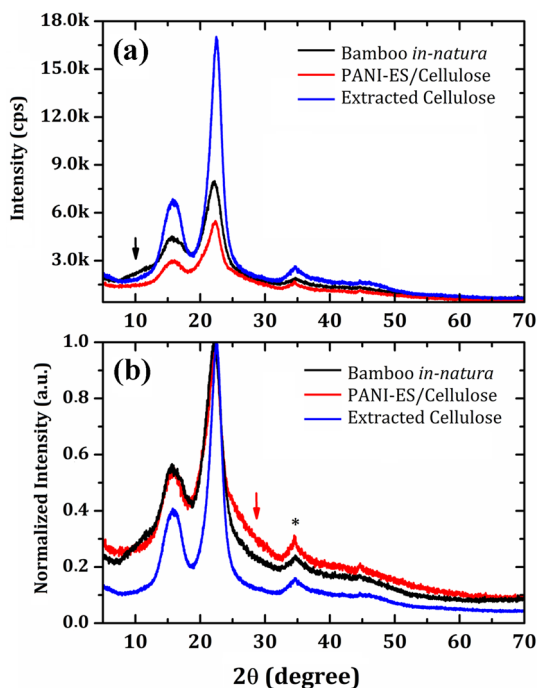


Fig. 1 XRD patterns of the bamboo *in-natura*, extracted cellulose and PANI-ES/Cellulose nanocomposite (a) under experimental conditions and (b) normalized

Fourier-transform Infrared Spectroscopy (FTIR)

FTIR spectrum was recorded using a Shimadzu IR Prestige-21 Spectrometer (TA Instruments) in the region $4000\text{--}500 \text{ cm}^{-1}$, resolution of 1 cm^{-1} and 64 scans. Pellets were prepared using KBr (1:100 w/w).

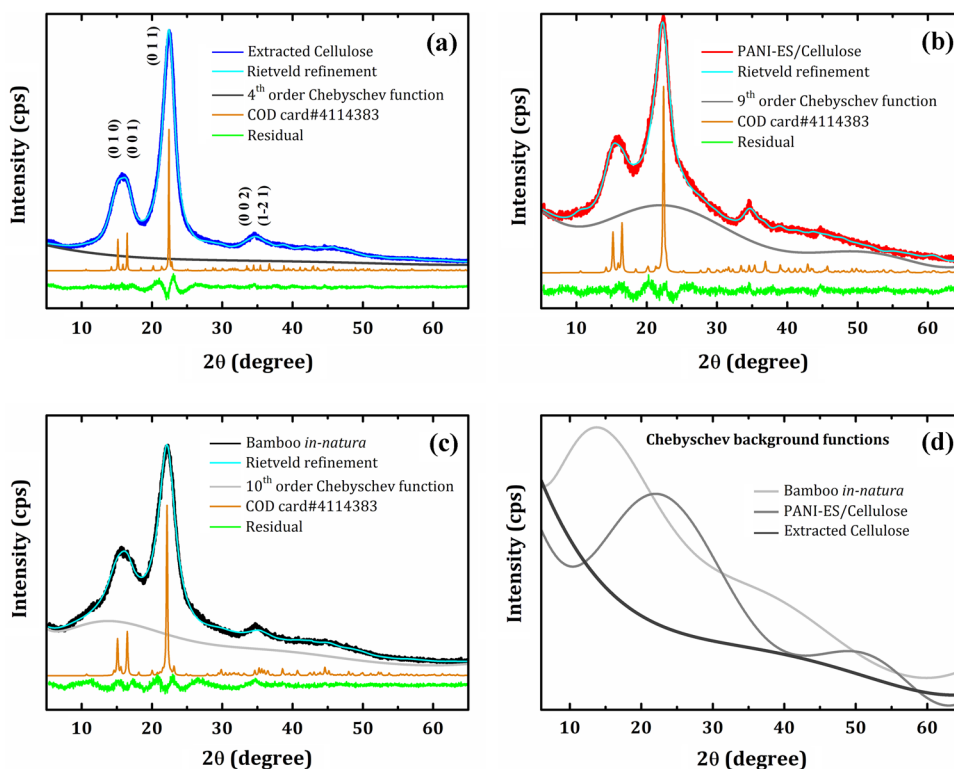
Thermogravimetric analysis (TG/dTG)

TG/dTG analyses were performed on a DTG-60H equipment using alumina crucibles and mass sample of 11.626 mg (bamboo *in-natura*), 8.732 mg (extracted cellulose) and 8.396 mg (PANI/Cellulose nanocomposite). The experiment was carried out under N_2 atmosphere (flux of 50 mL/min) at a heating rate of $10 \text{ }^\circ\text{C/min}$ in the range of $25\text{--}800 \text{ }^\circ\text{C}$.

Scanning electron microscopy (SEM)

SEM experiments were performed on a Carl Zeiss equipment, model Supra 35, using 1.0 kV at $25 \text{ }^\circ\text{C}$. Samples were placed on a carbon tape and recovered with a thin gold layer prior to analysis.

Fig. 2 Rietveld refinement performed using as initial parameters the COD card#4,114,383: **a** extracted cellulose, **b** PANI-ES/Cellulose nanocomposite, **c** bamboo *in-natura* and **d** Chebyshev background functions



Complex impedance spectroscopy (CIS)

A Solartron 1260 impedance analyzer was used for collecting data at room temperature. Disc-shape samples (2.10 mm thickness; 10 mm diameter) were prepared using a hydraulic press (1.5 tons) for 5 min. Measurements were performed at 0.5 V from 10 Hz to 10.0 MHz.

Results and discussion

X-ray diffraction and Rietveld refinement analysis

Figure 1a shows the XRD patterns of the bamboo *in-natura*, extracted cellulose and PANI-ES/Cellulose nanocomposite. Depending on the inter- and intramolecular interactions, as well as molecular orientations, cellulose can exist as different polymorphs or allomorphs (George and Sabapathi 2015). The diffraction patterns of cellulose in all samples were accurately represented by the triclinic structure of I_{α} -cellulose, considering that the diffraction peak at $2\theta = 16^{\circ}$ was composed of two broaden planes, $(-1\ 1\ 0)$ and $(1\ 1\ 0)$. As all measurements were performed under the same experimental conditions, the differences between the intensities of the XRD patterns were attributed to different crystallinity levels.

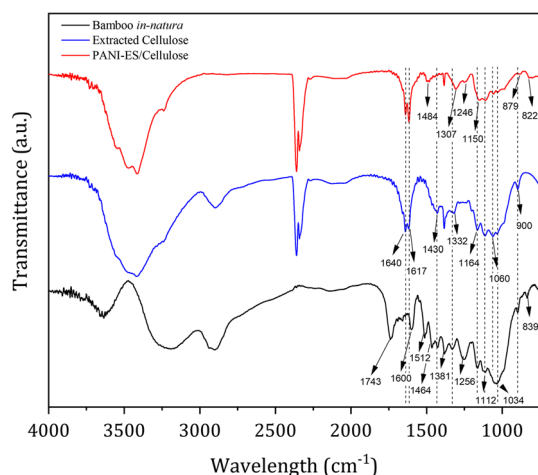
Naturally occurring bulk cellulose consists of highly ordered, crystalline regions coexisting with some disordered (amorphous) regions in varying proportions, depending on its source (George and Sabapathi 2015). A broaden halo around $2\theta \sim 10^{\circ}$ was observed in the XRD pattern of the bamboo *in-natura* (indicated by an arrow). This component corresponded to the naturally disordered structure of holocellulose. The XRD pattern of the PANI/Cellulose nanocomposite was considerably less intense, indicating that the polymerization of aniline over the extracted cellulose surface was effective, but resulting in marginal evidence of semi crystallinity.

A more detailed relation between samples can be guaranteed by removing the efficiency on which each sample scatters light due to its own crystallinity. For this reason, all XRD patterns were normalized by the intensity of the most intense peak, which was centered around $2\theta \sim 22.4^{\circ}$, as shown in Fig. 1b. Consequently, the cellulose peaks were substantially narrower than those found on the XRD pattern of the bamboo *in-natura*, indicating that those crystals are larger and more ordered. The peaks of the extracted cellulose were slightly shifted to higher angles, suggesting that its unit cell volume was marginally reduced as a result of internal stress effects (Nishiyama et al. 2003).

Data normalization procedure revealed important details on the diffraction pattern of the PANI-ES/Cellulose nanocomposite: The first observation concerns the angular region

Table 1 Rietveld refinement results performed for the bamboo *in-natura*, extracted cellulose, and PANI-ES/Cellulose nanocomposite

Sample	Lattice parameters	R_{wp}	χ^2	$D_{(011)}$ (Å)	$\epsilon_{(011)}$ (%)	Crystallinity (%)	Texture index
Extracted cellulose	$a = 10.177(7)$ Å $b = 6.623(3)$ Å $c = 5.931(3)$ Å $\alpha = 78.33(3)^\circ$ $\beta = 114.97(4)^\circ$ $\gamma = 118.15(3)^\circ$ $V = 319.5(2)$ Å ³	0.0371	3.296	36(9)	2.7 (9)	70	4.9
bamboo <i>in natura</i>	$a = 10.11(3)$ Å $b = 6.567(9)$ Å $c = 6.038(8)$ Å $\alpha = 76.9(1)^\circ$ $\beta = 117.1(1)^\circ$ $\gamma = 116.8(1)^\circ$ $V = 318.2(8)$ Å ³	0.0349	2.331	26(2)	3.7(7)	42	8.7
PANI/Cellulose nanocomposite	$a = 10.26(1)$ Å $b = 6.628(5)$ Å $c = 5.940(8)$ Å $\alpha = 78.10(5)^\circ$ $\beta = 114.95(8)^\circ$ $\gamma = 118.39(5)^\circ$ $V = 322.2(6)$ Å ³	0.0357	1.846	25(6)	4.0(7)	36	14.7
COD Card#4,114,383 [42]	$a = 10.400$ Å $b = 6.717$ Å $c = 5.962$ Å $\alpha = 80.37^\circ$ $\beta = 118.08^\circ$ $\gamma = 114.80^\circ$ $V = 333.3$ Å ³	–	–	–	–	–	–

**Fig. 3** FTIR spectra of the bamboo *in-natura*, extracted cellulose and PANI-ES/Cellulose nanocomposite

$2\theta = 25^\circ\text{--}33^\circ$, which corresponded to the distribution of interatomic distances of PANI-ES. After polymerization, the cellulose peaks were no longer shifted to larger angles,

returning to the initial angular position diffracted before extraction, overlapping the peaks of the bamboo *in-natura* even in width and shape. This result suggests that the cellulose crystals were relaxed, returning to their natural disorder. However, the PANI-ES/Cellulose nanocomposite presented a significant evidence of ordering in the peak at $2\theta \sim 34^\circ$ (indicated by an asterisk): it became relatively more intense and narrower. This evidence may indicate a considerable interaction between PANI-ES and cellulose crystals. The ability of the hydroxyl groups from cellulose to form strong hydrogen bonds is the main reason for some other properties (George and Sabapathi 2015).

A more accurate analysis was performed through Rietveld refinement. Figure 2 shows the Rietveld refinement performed using as initial parameters the crystallographic data from the COD card#4114383 (Crystallography Open Database – COD (Quirós et al. 2018)). The refined parameters are shown in Table 1. The unit cell volume of the extracted cellulose was 4% smaller than the indexed cellulose (initial parameters). This difference may be attributed to several reasons such as crystallite size variations resulting in different compressive forces from crystals and unit cells (Nishiyama et al. 2003).

The idealized XRD patterns (Lorentzians with $\text{FWHM} = 0.2^\circ$) were calculated using the Mercury software (Macrae et al. 2008) and shown in Fig. 2a–c (in orange). The peak centered at $2\theta \sim 16^\circ$ clearly corresponded to the overlapped planes (0 1 0) and (0 0 1), and the peak centered at $2\theta \sim 34^\circ$ resulted from the overlapping of several peaks. The ODF model was required for preferential orientation adjustments of these peaks: This effect on cellulose is a consequence of typically oriented fibers and can be estimated from the texture coefficient.

The extracted cellulose crystals presented half the value of the texture index of the bamboo *in-natura*, revealing that the extraction process of cellulose resulted in smaller and better oriented crystals. Furthermore, the *in-situ* polymerization of aniline over the cellulose fibers promoted a threefold increase in the orientation of the cellulose crystals in the nanocomposite form, increasing the intensity of the planes (0 0 2) and (1 -2 1).

Texture effects in cellulose affected the measurement of crystallinity percentage by the Segal method (Driemeier and Calligaris 2011) since the relative intensity between peaks was modified. Thus, the Rietveld refinement represents a tool to evaluate the background function. Rietveld refinements were performed using the smallest possible Chebyshev polynomials to fit all the non-crystalline details shown in Fig. 2d. Considering the extracted cellulose, a fourth-order polynomial was applied, while for the bamboo *in-natura* and the PANI-ES/Cellulose nanocomposite a higher-order polynomial was required. Applying the Segal's formula for the background function (I_{bckg}) and total areas (I_{total}), the crystallinity percentage [X_c (%)] was estimated by the following equation:

$$X_c(\%) = 100(I_{\text{total}} - I_{\text{bckg}}/I_{\text{total}}) \quad (8)$$

The obtained values are shown in Table 1. Atomic displacement and inelastic scattering effects were neglected. However, results were as expected: the extracted cellulose presented substantial crystallinity; the bamboo *in-natura* presented high holocellulose content, and the PANI-ES phase contributed with more than 60% of the X-ray scattering from the PANI-ES/Cellulose nanocomposite. The microstructural analysis from the peak (0 1 1) corroborated with the interaction between PANI-ES and cellulose as it indicates a high microstrain in all samples, and even larger in the nanocomposite form. On the other hand, the crystals were slightly different from each other although presenting nanometric dimensions.

FTIR analysis

FTIR spectra of the bamboo *in-natura*, extracted cellulose and PANI-ES/Cellulose nanocomposite are shown in Fig. 3.

The spectra of the extracted cellulose and nanocomposite are quite similar. However, the spectrum of the nanocomposite presented red shift of the peaks from cellulose.

Bands related to the -OH vibration were observed in the region from 3750 to 3000 cm^{-1} (Manzato et al. 2017; Kadivar et al. 2019; Qanytah et al. 2019; Wang et al. 2019a), resulting from the water associated with the hydroxyl groups present the main chain of cellulose in all samples.

The region from 3000 to 2700 cm^{-1} (Manzato et al. 2017; Kian et al. 2017; Kadivar et al. 2019) comprised the aliphatic C-H stretching from cellulose chains. The main region of interest for lignocellulosic materials ranged from 1800 to 800 cm^{-1} , where the main characteristic bands were identified.

The presence of hemicellulose in the bamboo *in-natura* was confirmed by the band at 1743 cm^{-1} , resulted from the C=O stretching of acetyl or carboxylic acid groups (Xu et al. 2013; Frone et al. 2017; Oliveira et al. 2017). Lignin bands were found at 1658 cm^{-1} , 1600 cm^{-1} and 1512 cm^{-1} , which corresponded to the C=C stretching vibrations of aromatic skeletal (Xu et al. 2013; Kian et al. 2017; Qanytah et al. 2019). The bands at 1464 cm^{-1} and 1425 cm^{-1} were related to the CH_2 bending, as well as CH_3 asymmetric deformation in lignin (Xu et al. 2013; Manzato et al. 2017). The band at 1256 cm^{-1} was assigned to the CO^- stretching in phenol-ether bond (Xu et al. 2013), while the bands at 1112 cm^{-1} and 839 cm^{-1} were assigned, respectively, to the C-H stretching in syringyl (Xu et al. 2013) and C=C stretching with an alkene functional group in lignin (Qanytah et al. 2019). The presence of cellulose was confirmed by the bands at 1430 cm^{-1} and 1381 cm^{-1} , which were related to C-H bending vibration and deformation, respectively (Xu et al. 2013; Razalli et al. 2017). The band at 1164 cm^{-1} represents one of the cellulose main bands and corresponded to the C-O-C pyranose ring skeletal vibration. The band at

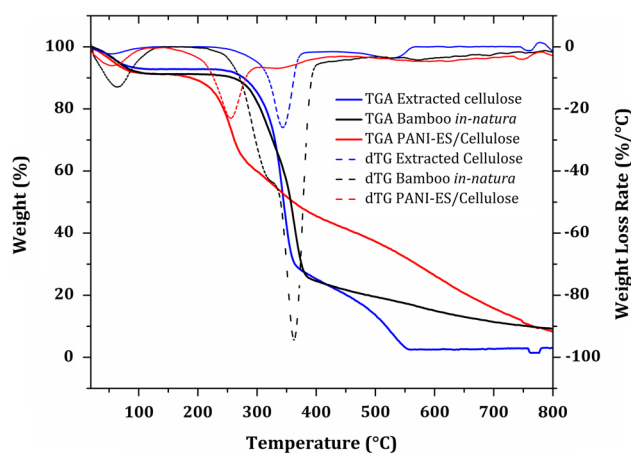


Fig. 4 TG/dTG curves of the bamboo *in-natura*, extracted cellulose and PANI-ES/Cellulose nanocomposite

1034 cm^{-1} was related to the C–OH bond in cellulose, and the band at 900 cm^{-1} is characteristic of β -1,4 glycosidic bonds in its skeletal (Xu et al. 2013; Frone et al. 2017; Kas-saye et al. 2017; Kian et al. 2017).

The cellulose extraction process removed significantly the hemicellulose and lignin contents, which was verified by the absence of the bands previously found on the bamboo *in-natura* spectrum at 1743 cm^{-1} for hemicellulose, and at 1658 cm^{-1} , 1600 cm^{-1} , 1512 cm^{-1} , 1464 cm^{-1} , 1256 cm^{-1} , and 839 cm^{-1} (Xu et al. 2013; Frone et al. 2017; Manzato et al. 2017; Kian et al. 2017) for lignin. The removal of hemicellulose and lignin allowed better visualization of the cellulose bands due to the exposure of the cellulose fiber structure, which is very hydrophilic due to the presence of hydroxyl groups. This exposure resulted in superficial and intermolecular water absorption, which were confirmed by the characteristic bands at 1640 cm^{-1} and 1617 cm^{-1} (Kian et al. 2017) in the spectra of the extracted cellulose and PANI-ES/Cellulose nanocomposite samples.

Some cellulose bands presented a red shift in the nanocomposite from 1164 cm^{-1} to 1150 cm^{-1} , and from 900 cm^{-1} to 879 cm^{-1} probably due to chemical interaction between PANI-ES and cellulose, as found in other reports (Müller et al. 2011; Razalli et al. 2017) and previously discussed on the XRD results. In contrast to carbohydrates of lower molar mass, the reactions and properties of cellulose are determined by intermolecular interactions, crosslinking reactions, chain lengths, chain length distribution, as well as by the distribution of functional groups on the repeating units and along the polymer chains (Klemm et al. 2005). When the aniline was allowed to polymerize over the carbohydrate surface, a reduction of the intensity of cellulose bands between 1500 cm^{-1} and 900 cm^{-1} was observed, including the disappearance of the bands at 1430 cm^{-1} and 1332 cm^{-1} , both related to the C–H bending and in-plane deformation (Xu et al. 2013; Razalli et al. 2017; Kian et al. 2017). This result may be related to the recovering of the fibers by the conjugated polymer (Müller et al. 2011; Razalli et al. 2017).

Furthermore, the presence of PANI-ES was confirmed by the bands at 1484 cm^{-1} due the ring stretching vibration of benzenoid rings (Sanches et al. 2014), and at 1246 cm^{-1} from the C–N stretching of a secondary aromatic amine (Sanches et al. 2015; Ferreira and Sanches 2017). The bands at 822 cm^{-1} and 789 cm^{-1} resulted from the N–H⁺ structure formed during the protonation and to the 1,4-substituted benzene (Liu et al. 2014; Ferreira and Sanches 2017).

TGA/dTG analyses

TGA/dTG analyses were useful to describe the thermal behavior of the bamboo *in-natura*, extracted cellulose and PANI-ES/Cellulose nanocomposite, as shown in Figs. 4.

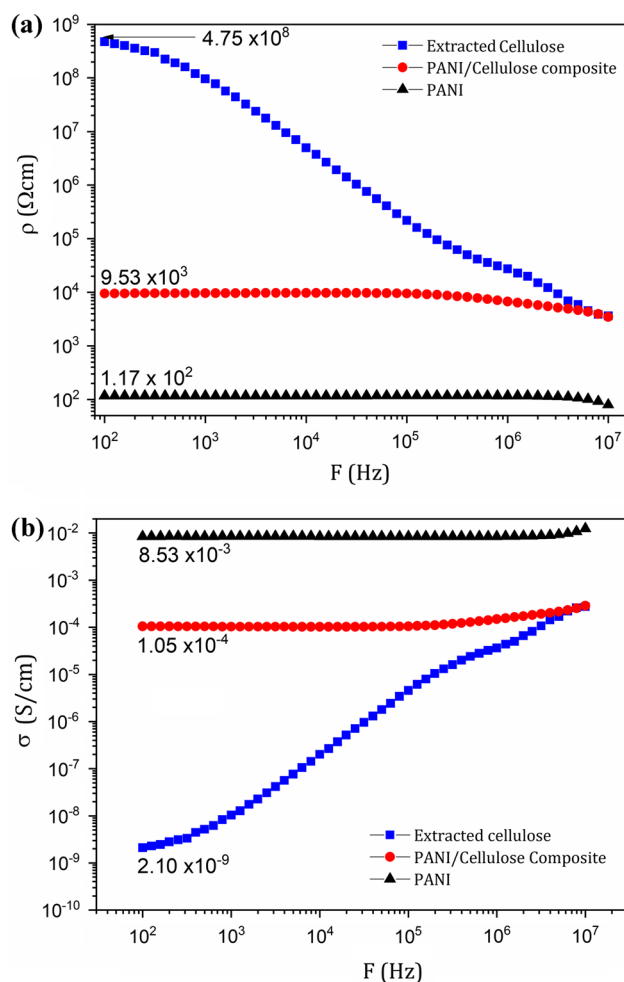


Fig. 5 **a** Resistivity (ρ) and **b** ac electrical conductivity (σ_{ac}) as a function of the frequency for the extracted cellulose, pure PANI-ES and PANI-ES/Cellulose nanocomposite.

Lignocellulosic materials are mainly composed of hemicellulose, cellulose, and lignin. These materials present specific behaviors, and lignin is the most thermally stable and degrades gradually, while hemicellulose and cellulose have overlapping degradation events due to the similar range of their temperature degradation (Yang et al. 2007).

The bamboo *in-natura* presented three well-defined thermal events. The first one was observed from 21 $^{\circ}\text{C}$ to 134 $^{\circ}\text{C}$, and was assigned to the moisture release, representing 9% of mass loss. This thermal event can also be attributed to the release of waxes and resins (Chen and Kuo 2010). The second thermal event was consecutive and represented the start of the hemicellulose degradation, followed by the degradation of cellulose until 335 $^{\circ}\text{C}$, resulting in 27% of mass loss. The third thermal event was observed from 342 $^{\circ}\text{C}$ to 490 $^{\circ}\text{C}$, and corresponded to the lignin degradation (Zhang et al. 2015), resulting in 44% of mass loss.

The extracted cellulose presented three well-defined thermal events. The first one was observed from 21 °C to 100 °C and was assigned to the moisture release, resulting in 7% of mass loss. The second and third thermal events were overlapped and started at 265 °C, which was the degradation temperature of hemicellulose. However, the temperature at which started the cellulose degradation was not possible to be defined due to the overlapping of the thermal events. However, the final temperature of cellulose degradation was verified at 355 °C, resulting in a mass loss of 63% (Kabir et al. 2013). The degradation of lignin was verified from 365 °C to 571 °C, resulting in mass loss of 27.3%.

The PANI-ES/Cellulose nanocomposite presented four well-defined thermal events. The first one was verified from 25 °C to 100 °C and was assigned to the moisture release, resulting in 8% of mass loss. The second thermal event at 157 °C presented mass loss of 30% and was attributed to the degradation of hemicellulose as well as to the release of the Cl^- counterions from PANI-ES. The third thermal event started at 282 °C resulting in mass loss of 17%. The thermal stability of the PANI-ES/Cellulose nanocomposite cellulose revealed to be lower than the extracted cellulose. Some reports have shown an improvement of the thermal stability of cellulose in the form of a nanocomposite, assigning a delaying mass loss effect due to the presence of conducting polymer (Lee et al. 2012; He et al. 2016; Raghunathan et al. 2017). However, once the thermal stability of the samples was evaluated varying the temperature, these expected results mentioned above were not observed. Therefore, the lower stability of the nanocomposite occurs probably due to the presence of the counterion present in the polymer chains which accelerated the degradation process (Feitosa et al. 2021). As observed from the XRD results, a considerable chemical interaction between PANI-ES and cellulose was observed and also may be influenced on the thermal stability of the nanocomposite. The last thermal event was verified from 403 °C to 700 °C and was attributed to the degradation of the remaining lignin, as well as to the total rupture of the polymer chains and carbonized polymer fragments (Wang and Jing 2008; Siaeira et al. 2009; Lou et al. 2016).

Complex impedance spectroscopy analysis (CIS)

Figure 5 shows the electrical response of pure PANI-ES, extracted cellulose and PANI-ES/Cellulose nanocomposite in terms of resistivity (ρ) (Fig. 5a) and *ac* electrical conductivity (σ_{ac}) (Fig. 5b) as a function of frequency at room temperature.

The extracted cellulose presented the highest resistivity value at low frequencies ($4.78 \times 10^8 \Omega \cdot \text{cm}$), with 5 to 6 orders of magnitude greater than those observed in PANI-ES/Cellulose nanocomposite ($9.53 \times 10^3 \Omega \cdot \text{cm}$) and pure PANI-ES ($1.17 \times 10^2 \Omega \cdot \text{cm}$). The extracted cellulose presented high

frequency dependence, decreasing the resistivity values when the frequency was increased. This behavior is typical of insulating materials (Raja et al. 2004). However, the pure PANI-ES and PANI-ES/Cellulose nanocomposite presented almost constant behavior along the frequency variation. The lowest resistivity value was observed in the pure PANI-ES, as expected (Sanches et al. 2013; Da Silva et al. 2014; Nazari et al. 2015; Wang et al. 2018).

The results of *ac* conductivity (σ_{ac}) were similar to those of resistivity in terms of behavior. Pure PANI-ES and PANI-ES/Cellulose nanocomposite presented σ_{ac} almost constant along the frequency variation, which was accompanied by a dispersion of conductivity when the frequency was increased. The *dc* conductivity values (σ_{dc}) were found around $8.53 \times 10^{-3} \text{ S/cm}$, $1.05 \times 10^{-4} \text{ S/cm}$ and $2.10 \times 10^{-9} \text{ S/cm}$ for pure PANI-ES, PANI-ES/Cellulose nanocomposite and extracted cellulose, respectively. Deviations were determined below 3%.

The polymerization of aniline over the extracted cellulose surface did not considerably decrease the *dc* conductivity (σ_{dc}), reducing only 1 order of magnitude when compared to the pure PANI-ES. It was expected that the decrease of electrical conductivity would be greater since cellulose is a highly resistive material. However, the fashion at which PANI-ES recovered the cellulose surface (as discussed on the XRD and SEM results), forming a complete film coating the cellulose fibers, may be related to the high electrical conductivity observed in the PANI-ES/Cellulose nanocomposite. This result was also probably due to a possible chemical interaction between cellulose fibers and PANI-ES: cellulose fibers may have acted as a pathway for polymerization, probably orienting the polymer growth on its surface due to the interaction between both phases. For this reason, this recovering may have contributed to facilitate the transport of charge carriers along the fibers, since the polymerization over them may have resulted in better alignment of the polymer chains.

The electrical conductivity values of nanocomposites constituted of polyaniline and cellulose depend on a number of factors, including (i) the degree of polymer doping and the type of dopant acids, (ii) the content of polymer in the nanocomposite, (iii) the methodology of the nanocomposite preparation, as well as (iv) the method used for electrical conductivity measurements (Mo et al. 2009; He et al. 2016). He et al. (He et al. 2016) prepared a nanocomposite based on PANI and cellulose extracted from *Phyllostachys nidularia*. A conductivity value of $8.6 \times 10^{-5} \text{ S/cm}$ was obtained when the content of PANI was 5 wt%. However, when the loading content increased to 30 wt%, the composite conductivity was significantly enhanced to $4.3 \times 10^{-2} \text{ S/cm}$. Clearly, the electrical conductivity of the composite increased accordingly with increased PANI content. Mo et al. (Mo et al. 2009) reported that PANI/Cellulose composites prepared using

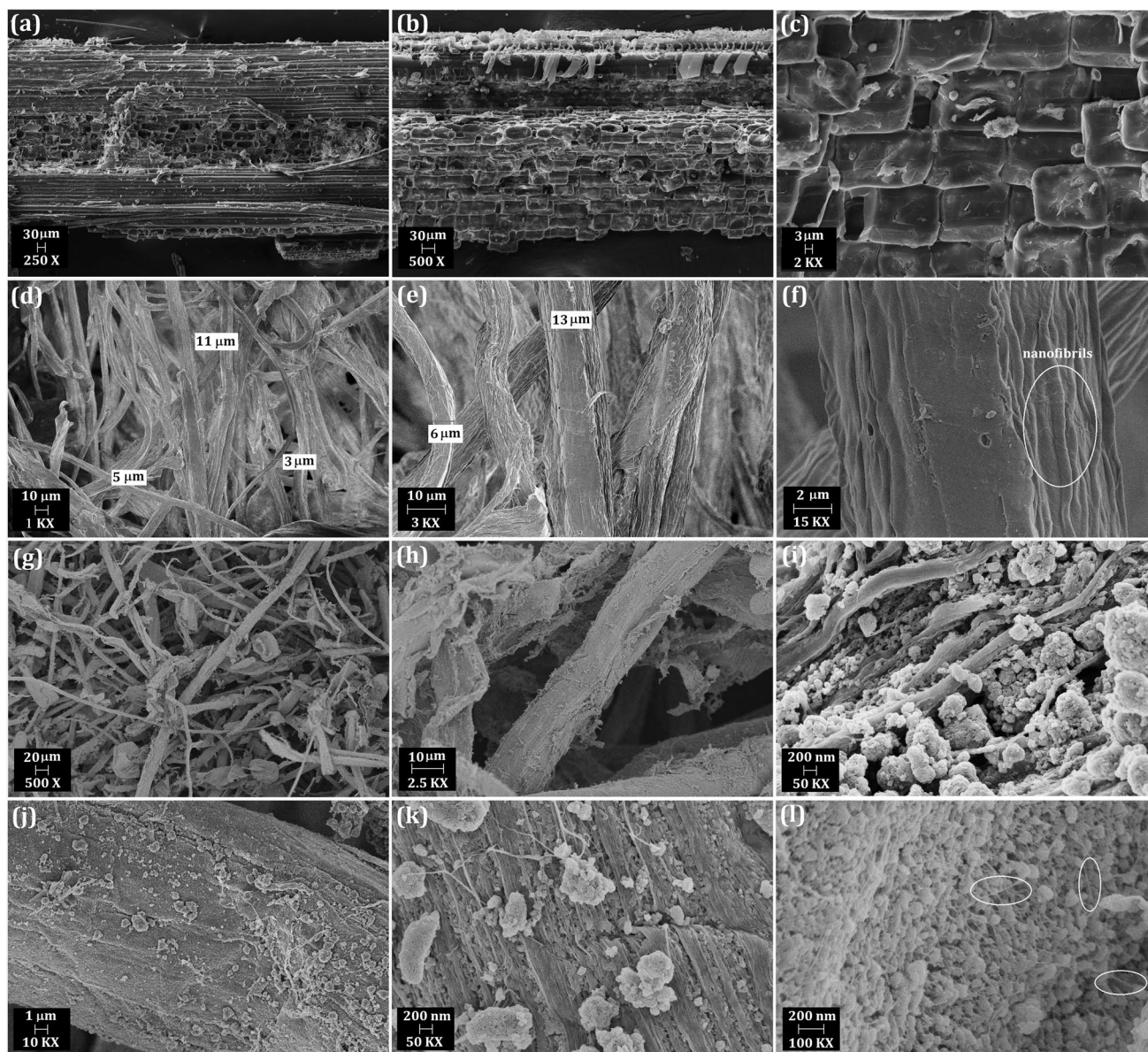


Fig. 6 a–c SEM images of the bamboo *in-natura*, d–f extracted cellulose and g–l PANI-ES/Cellulose nanocomposite.

di-basic acids exhibited more excellent conductivity than the composites prepared using the monobasic acids. Furthermore, both the PANI content and the electrical conductivity increased with an increase of the amount of PANI.

On the other hand, the mechanisms of charge conduction in nanocomposites constituted of PANI and cellulose are still not completely understood, precisely because of the diversity of factors affecting electrical conductivity (Martens et al. 2001; Prigodin and Epstein 2003; Zhou et al. 2004; Leite et al. 2008). It is, nevertheless, widely accepted that in the PANI structure the doped molecules are not uniformly distributed, but rather agglomerated into conducting islands (Jeon et al. 1992; Bianchi et al. 1999). In polymers we refer

as metallic grains the crystalline domains of well-packed chains, with delocalized electrons, dispersed in a disordered chain. The chains in the crystalline regions (pure PANI-ES and PANI-ES/Cellulose nanocomposite) should be better aligned, which would increase electron delocalization (Leite et al. 2008). Then, intergrain resonance tunneling occurs across the strongly localized states in the disordered media (Prigodin and Epstein 2003).

Scanning Electron Microscopy (SEM) analysis

The morphology of the bamboo *in-natura* is shown in Fig. 6a–c. The ground tissue of a bamboo culm consists of

parenchyma cells, with embedded vascular bundles composed of metaxylem vessels, sieve tubes with companion cells, and fibers (Liese 1998). Figure 6a–c shows the culm in a longitudinal section. In Fig. 6a, parenchyma cells were observed between fibers bundles. Figure 6b shows the parenchyma cells closed to vascular bundles, probably one of the metaxylem vessel, and Fig. 6c presents the parenchyma cells with remaining few starch granules. The surface roughness can be attributed mainly to lignin, hemicellulose, as well as non-cellulosic materials (Khan et al. 2020).

The extracted cellulose presented micro-sized fibers with highly rough surface, as shown in Fig. 6d–f. However, this morphology was completely different from that observed in the bamboo *in-natura*, suggesting that hemicellulose and lignin were successfully removed together with some other extractives during the chemical treatments (Deepa et al. 2015). These images revealed several nanofibrils, which may be a result of the dissolution of the plant components during the alkaline treatment and bleaching processes, resulting in the separation of the cellulose filaments presented in the cell wall layers. Each separated fiber revealed a crumpled paper-like morphology (better visualized in Fig. 6f). The fibers of the extracted cellulose presented a range of diameter size. Figure 6d–e shows that some fibers presented diameters from 3 to 13 μm . The distribution of the diameter size was not possible to be estimated due to the high fiber's overlapping. Furthermore, as highlighted in Fig. 6f, the extracted cellulose fibers can be composed of several nanofibrils.

Figure 6g–i shows the morphology of PANI-ES/Cellulose nanocomposite. Figure 6g–h shows that the cellulose fibers were significantly recovered by PANI-ES, indicating that the polymer acted as reinforcement of the cellulose matrix. Figure 6i revealed cellulose fibers with even smaller diameters (nanofibrils), which were also totally covered. Figure 6i–l shows that PANI-ES presented globular nanostructure of almost spherical shape (Fig. 6l), as well as a tendency of polymerization on the surface of the cellulose fibers, acting as a polymeric film. These polymeric globular nanostructures seem to be connected by polymeric nanofibers, as highlighted in Fig. 6l. These results are also in agreement with the previous analysis of electrical conductivity: the *in-situ* polymerization of aniline modified the surface of the cellulose fibers, acting as a pathway for polymerization, probably orienting the polymer growth on its surface.

Conclusions

Cellulose from *B. vulgaris* was successfully extracted through the proposed chemical methodology. The polymerization of aniline on the surface of the extracted cellulose was carried out to obtain a conducting nanocomposite. Considering cellulose as a highly resistive material, the

electrical conductivity of the obtained nanocomposite was not considerably reduced. This fact was due to the polymerization mechanism over the cellulose surface: the *in-situ* oriented-polymerization of aniline in the presence of the extracted cellulose resulted in some interaction between both phases. The microstructural analysis strongly suggested the interaction between PANI-ES and cellulose, indicating high microstrain for all samples, and even larger in the nanocomposite form. SEM images revealed that the fashion at which PANI-ES recovered the cellulose surface may have allowed the transport of charges in the nanocomposite. This behavior becomes important for proposing new technological applications for cellulose-based nanocomposites, since the incorporation of a conjugated polymer can reveal new physicochemical and mechanical properties.

Acknowledgements This work was supported by CNPq (Conselho Nacional de Desenvolvimento Científico e Tecnológico—Grant Numbers 403496/2013-6, 305161/2017-2, 401508/2016-1 and 305161/2017-2), Fundação de Amparo à Pesquisa do Estado do Amazonas (FAPEAM), Laboratório de Pesquisa em Materiais (LabMat/UFAM) and Laboratório de Processamento de Materiais Tecnológicos (LPMat/UFAM).

Author contributions Laiane Souza da Silva carried out the experiment, verified the analytical methods and performed the computations. Bianca de Andrade Feitosa, Ana Luisa Farias Rocha, Suzan Xavier Lima and Matheus Moraes Biondo contributed to the interpretation of the FTIR and TG/dTG results. Sergio Michielon de Souza and Camila da Costa Pinto contributed to the XRD analysis. Cláudia de Lima Nogueira contributed to the interpretation of the SEM results. Yurimiler Leyet Ruiz contributed to the measurements and interpretation of the electrical conductivity data. Edgar A. Sanches conceived the original idea, supervised the findings of this work and wrote the manuscript with support from Pedro H. Campelo. All authors discussed the results and contributed to the final manuscript.

Funding This work was supported by CNPq (Conselho Nacional de Desenvolvimento Científico e Tecnológico—Grant Numbers 403496/2013-6, 305161/2017-2, 401508/2016-1 and 305161/2017-2), Fundação de Amparo à Pesquisa do Estado do Amazonas (FAPEAM), Laboratório de Pesquisa em Materiais (LabMat/UFAM) and Laboratório de Processamento de Materiais Tecnológicos (LPMat/UFAM).

Declarations

Conflicts of interest There are no conflicts of interest.

Availability of data and material (data transparency) Data available within the article or its supplementary materials.

Code availability (software application or custom code) Not Applicable.

References

Alonso E, Faria M, Mohammadkazemi F et al (2018) Conductive bacterial cellulose-polyaniline blends: Influence of the matrix and

- synthesis conditions. *Carbohydr Polym* 183:254–262. <https://doi.org/10.1016/j.carbpol.2017.12.025>
- Bianchi RF, Leal Ferreira GF, Lepienski CM, Faria RM (1999) Alternating electrical conductivity of polyaniline. *J Chem Phys* 110:4602–4607. <https://doi.org/10.1063/1.478341>
- Cao Z, Li W, Suo X et al (2020) Structures and cyclization behaviors of gel-spun cellulose/polyacrylonitrile composite fibers. *Polym Test* 81:106276. <https://doi.org/10.1016/j.polymertesting.2019.106276>
- Chen WH, Kuo PC (2010) A study on torrefaction of various biomass materials and its impact on lignocellulosic structure simulated by a thermogravimetry. *Energy* 35:2580–2586. <https://doi.org/10.1016/j.energy.2010.02.054>
- Da Silva JSL, Oliveira MDL, De Melo CP, Andrade CAS (2014) Impedimetric sensor of bacterial toxins based on mixed (Concanavalin A)/polyaniline films. *Colloids Surf B Biointerfaces* 117:549–554. <https://doi.org/10.1016/j.colsurfb.2013.12.057>
- de Feitosa BA, Rocha ALF, Lima SX et al (2021) Nanocomposites based on the cellulose extracted from the Amazon *Peperomia pellucida* and polyaniline derivatives: structural and thermal properties. *Chem Pap* 75:1809–1821. <https://doi.org/10.1007/s11696-020-01435-4>
- de Oliveira JP, Bruni GP, Lima KO et al (2017) Cellulose fibers extracted from rice and oat husks and their application in hydrogel. *Food Chem* 221:153–160. <https://doi.org/10.1016/j.foodchem.2016.10.048>
- De Figueiredo LP, Ferreira FF (2014) The rietveld method as a tool to quantify the amorphous amount of microcrystalline cellulose. *J Pharm Sci* 103:1394–1399. <https://doi.org/10.1002/jps.23909>
- Deepa B, Abraham E, Cordeiro N et al (2015) Utilization of various lignocellulosic biomass for the production of nanocellulose: a comparative study. *Cellulose* 22:1075–1090. <https://doi.org/10.1007/s10570-015-0554-x>
- Driemeier C, Calligaris GA (2011) Theoretical and experimental developments for accurate determination of crystallinity of cellulose i materials. *J Appl Crystallogr* 44:184–192. <https://doi.org/10.1107/S0021889810043955>
- Fei G, Wang Y, Wang H et al (2019) Fabrication of bacterial cellulose/polyaniline nanocomposite paper with excellent conductivity, strength, and flexibility. *ACS Sustain Chem Eng* 7:8215–8225. <https://doi.org/10.1021/acssuschemeng.8b06306>
- Ferreira AA, Sanches EA (2017) Multimorphologies of hydrochloride polyaniline synthesized by conventional and interfacial polymerization. *J Mol Struct* 1143:294–305. <https://doi.org/10.1016/j.molstruc.2017.04.104>
- Frone AN, Chiulan I, Panaitescu DM et al (2017) Isolation of cellulose nanocrystals from plum seed shells, structural and morphological characterization. *Mater Lett* 194:160–163. <https://doi.org/10.1016/j.matlet.2017.02.051>
- George J, Sabapathi SN (2015) Cellulose nanocrystals: Synthesis, functional properties, and applications. *Nanotechnol Sci Appl* 8:45–54. <https://doi.org/10.2147/NSA.S64386>
- Gurjanov OP, Ibragimova NN, Gnezdilov OI, Gorshkova TA (2008) Polysaccharides, tightly bound to cellulose in cell wall of flax bast fibre: Isolation and identification. *Carbohydr Polym* 72:719–729. <https://doi.org/10.1016/j.carbpol.2007.10.017>
- Hajlaoui O, Khiari R, Ajili L et al (2020) Design and Characterization of Type I Cellulose-Polyaniline Composites from Various Cellulose Sources: A Comparative Study. *Chem Africa*. <https://doi.org/10.1007/s42250-020-00148-1>
- He W, Tian J, Li J et al (2016) Characterization and properties of cellulose nanofiber/polyaniline film composites synthesized through in Situ polymerization. *BioResources* 11:8535–8547
- He J, Li N, Bian K, Piao G (2019) Optically active polyaniline film based on cellulose nanocrystals. *Carbohydr Polym* 208:398–403. <https://doi.org/10.1016/j.carbpol.2018.12.091>
- Hernandez CC, Ferreira FF, Rosa DS (2018) X-ray powder diffraction and other analyses of cellulose nanocrystals obtained from corn straw by chemical treatments. *Carbohydr Polym* 193:39–44. <https://doi.org/10.1016/j.carbpol.2018.03.085>
- Jeon D, Kim J, Gallagher MC, Willis RF (1992) Scanning tunneling spectroscopic evidence for granular metallic conductivity in conducting polymeric polyaniline. *Science* 256:1662–1664. <https://doi.org/10.1126/science.256.5064.1662>
- Kabir MM, Wang H, Lau KT, Cardona F (2013) Effects of chemical treatments on hemp fibre structure. *Appl Surf Sci* 276:13–23. <https://doi.org/10.1016/j.apsusc.2013.02.086>
- Kadivar M, Gauss C, Mármol G et al (2019) The influence of the initial moisture content on densification process of *D. asper bamboo*: Physical-chemical and bending characterization. *Constr Build Mater* 229:116896. <https://doi.org/10.1016/j.conbuildmat.2019.116896>
- Kassaye S, Pant KK, Jain S (2017) Hydrolysis of cellulosic bamboo biomass into reducing sugars via a combined alkaline solution and ionic liquid pretreatment steps. *Renew Energy* 104:177–184. <https://doi.org/10.1016/j.renene.2016.12.033>
- Khan MN, Rehman N, Sharif A et al (2020) Environmentally benign extraction of cellulose from dunchi fiber for nanocellulose fabrication. *Int J Biol Macromol* 153:72–78. <https://doi.org/10.1016/j.ijbiomac.2020.02.333>
- Kian LK, Jawaid M, Ariffin H, Alothman OY (2017) Isolation and characterization of microcrystalline cellulose from roselle fibers. *Int J Biol Macromol* 103:931–940. <https://doi.org/10.1016/j.ijbiomac.2017.05.135>
- Klemm D, Heublein B, Fink HP, Bohn A (2005) Cellulose: fascinating biopolymer and sustainable raw material. *Angew Chemie Int Ed* 44:3358–3393. <https://doi.org/10.1002/anie.200460587>
- Larson AC, Von Dreele RB (2004) General structure analysis system (GSAS). *Los Alamos Natl Lab Rep LAUR* 748:86–748
- Lee BH, Kim HJ, Yang HS (2012) Polymerization of aniline on bacterial cellulose and characterization of bacterial cellulose/polyaniline nanocomposite films. *Curr Appl Phys* 12:75–80. <https://doi.org/10.1016/j.cap.2011.04.045>
- Leite FL, Alves WF, Mir M et al (2008) TEM, XRD and AFM study of poly(o-ethoxyaniline) films: New evidence for the formation of conducting islands. *Appl Phys A Mater Sci Process* 93:537–542. <https://doi.org/10.1007/s00339-008-4686-9>
- Liese W (1998) *The Anatomy of Bamboo Culms*. Intl Network for Bamboo & Rattan, Beijing
- Liu DY, Sui GX, Bhattacharyya D (2014) Synthesis and characterisation of nanocellulose-based polyaniline conducting films. *Compos Sci Technol* 99:31–36. <https://doi.org/10.1016/j.compscitech.2014.05.001>
- Liu Y, Lv X, Bao J et al (2019) Characterization of silane treated and untreated natural cellulosic fibre from corn stalk waste as potential reinforcement in polymer composites. *Carbohydr Polym* 218:179–187. <https://doi.org/10.1016/j.carbpol.2019.04.088>
- Liu J, Wang H, Lin Z (2019) Preparation, structure and performances of cross-linked regenerated cellulose fibers. *Wuhan Univ J Nat Sci* 24(1):1–7
- Lou CW, Huang CL, Pan YJ et al (2016) Crystallization, mechanical, and electromagnetic properties of conductive polypropylene/SEBS composites. *J Polym Res*. <https://doi.org/10.1007/s10965-016-0979-4>
- Luo Y, Kong D, Jia Y et al (2013) Self-assembled graphene@PANI nanoworm composites with enhanced supercapacitor performance. *RSC Adv* 3:5851–5859. <https://doi.org/10.1039/c3ra00151b>
- Macrae CF, Bruno IJ, Chisholm JA et al (2008) Mercury CSD 2.0 - New features for the visualization and investigation of crystal structures. *J Appl Crystallogr* 41:466–470. <https://doi.org/10.1107/S0021889807067908>

- Manzato L, Rabelo LCA, de Souza SM et al (2017) New approach for extraction of cellulose from tucumã's endocarp and its structural characterization. *J Mol Struct* 1143:229–234. <https://doi.org/10.1016/j.molstruc.2017.04.088>
- Martens HCF, Reedijk JA, Brom HB et al (2001) Metallic state in disordered quasi-one-dimensional conductors. *Phys Rev B* 63:073203. <https://doi.org/10.1103/PhysRevB.63.073203>
- Mccusker LB, Von DRB, Cox DE et al (1999) Rietveld refinement guidelines. *J Appl Cryst* 32:36–50. <https://doi.org/10.1107/S0021889898009856>
- Mo ZL, Zhao ZL, Chen H et al (2009) Heterogeneous preparation of cellulose-polyaniline conductive composites with cellulose activated by acids and its electrical properties. *Carbohydr Polym* 75:660–664. <https://doi.org/10.1016/j.carbpol.2008.09.010>
- Moon RJ, Martini A, Nairn J et al (2011) Cellulose nanomaterials review: Structure, properties and nanocomposites. *Chem Soc Rev* 40(7):3941–3994
- Müller D, Rambo CR, Recouvreur DOS et al (2011) Chemical in situ polymerization of polypyrrole on bacterial cellulose nanofibers. *Synth Met* 161:106–111. <https://doi.org/10.1016/j.synthmet.2010.11.005>
- Nazari M, Kashanian S, Rafipour R (2015) Laccase immobilization on the electrode surface to design a biosensor for the detection of phenolic compound such as catechol. *Spectrochim Acta - Part A Mol Biomol Spectrosc* 145:130–138. <https://doi.org/10.1016/j.saa.2015.01.126>
- Nishiyama Y, Sugiyama J, Chanzy H, Langan P (2003) Crystal structure and hydrogen bonding system in cellulose I α from synchrotron X-ray and Neutron Fiber Diffraction. *J Am Chem Soc* 125:14300–14306. <https://doi.org/10.1021/ja037055w>
- Palaniappan S, Devi SL (2008) Novel chemically synthesized polyaniline electrodes containing a fluoroboric acid dopant for supercapacitors. *J Appl Polym Sci* 107:1887–1892. <https://doi.org/10.1002/app.27228>
- Pecharsky VK, Zavaliy PY (2009) *Fundamentals of Powder Diffraction and Structural Characterization of Materials*. Springer, US, Boston, MA
- Picanço WM, Feitosa BDA, da Silva NG et al (2018) Aniline-oriented polymerization over nano-SiO₂ particles. *J Mol Struct* 1167:118–126. <https://doi.org/10.1016/j.molstruc.2018.04.087>
- Prigodin VN, Epstein AJ (2003) Quantum hopping in metallic polymers. *Phys B Condens Matter* 338:310–317. <https://doi.org/10.1016/j.physb.2003.08.011>
- Qanytah SK, Fahma F, Pari G (2019) Structure analysis of three non-wood materials for liner paper. *Nord Pulp Pap Res J* 34:453–466. <https://doi.org/10.1515/npprj-2019-0043>
- Quirós M, Gražulis S, Girdzijauskaitė S et al (2018) Using SMILES strings for the description of chemical connectivity in the Crystallography Open Database. *J Cheminform* 10:23. <https://doi.org/10.1186/s13321-018-0279-6>
- Raghunathan SP, Narayanan S, Poulou AC, Joseph R (2017) Flexible regenerated cellulose/polypyrrole composite films with enhanced dielectric properties. *Carbohydr Polym* 157:1024–1032. <https://doi.org/10.1016/j.carbpol.2016.10.065>
- Raja V, Sharma AK, Narasimha Rao VVR (2004) Impedance spectroscopic and dielectric analysis of PMMA-CO-P4VPNO polymer films. *Mater Lett* 58:3242–3247. <https://doi.org/10.1016/j.matlet.2004.05.061>
- Razalli RL, Abdi MM, Tahir PM et al (2017) Polyaniline-modified nanocellulose prepared from Semantan bamboo by chemical polymerization: preparation and characterization. *RSC Adv* 7:25191–25198. <https://doi.org/10.1039/C7RA03379F>
- Rietveld HM (1967) Line profiles of neutron powder-diffraction peaks for structure refinement. *Acta Crystallogr* 22:151–152. <https://doi.org/10.1107/S0365110X67000234>
- Sanches EA, Soares JC, Mafud AC et al (2013) Structural and morphological characterization of chloride salt of conducting poly(o-methoxyaniline) obtained at different time synthesis. *J Mol Struct* 1039:167–173. <https://doi.org/10.1016/j.molstruc.2012.12.025>
- Sanches EA, Da Silva JMS, Ferreira JMDO et al (2014) Structural and Morphological Characterization of Nanostructured Polyaniline Emeraldine-base form (EB-PANI). *J Mol Struct* 1074:732–737. <https://doi.org/10.1016/j.molstruc.2014.05.046>
- Sanches EA, Carolino AS, Santos AL et al (2015) The use of Le Bail Method to analyze the semicrystalline pattern of a nanocomposite based on polyaniline emeraldine-salt form and α -Al₂O₃. *Adv Mater Sci Eng* 2015:1–8
- Sangamithirai D, Narayanan V, Muthuraaman B, Stephen A (2015) Investigations on the performance of poly(o-anisidine)/graphene nanocomposites for the electrochemical detection of NADH. *Mater Sci Eng C* 55:579–591. <https://doi.org/10.1016/j.msec.2015.05.066>
- Sharifi H, Zabihzadeh M, Ghorbani M (2018) The application of response surface methodology on the synthesis of conductive polyaniline/cellulosic fiber nanocomposites. *Carbohydr Polym* 194:384–394. <https://doi.org/10.1016/j.carbpol.2018.04.083>
- Siaueira G, Bras J, Dufresne A (2009) Cellulose whiskers versus microfibrils: Influence of the nature of the nanoparticle and its surface functionalization on the thermal and mechanical properties of nanocomposites. *Biomacromol* 10:425–432. <https://doi.org/10.1021/bm801193d>
- Stephens PW (1999) Phenomenological model of anisotropic peak broadening in powder diffraction. *J Appl Crystallogr* 32:281–289. <https://doi.org/10.1107/S0021889898006001>
- Svenningsson L, Lin Y, Karlsson M et al (2019) Molecular Orientation Distribution of Regenerated Cellulose Fibers Investigated with Polarized Raman Spectroscopy. *Macromolecules* 52:3918–3924. <https://doi.org/10.1021/acs.macromol.9b00520>
- Tanpichai S, Witayakran S, Srimarut Y et al (2019) Porosity, density and mechanical properties of the paper of steam exploded bamboo microfibrils controlled by nanofibrillated cellulose. *J Mater Res Technol* 8:3612–3622. <https://doi.org/10.1016/j.jmrt.2019.05.024>
- Thompson P, Cox DE, Hastings JB (1987) Rietveld refinement of Debye-Scherrer synchrotron X-ray data from Al₂O₃. *J Appl Crystal* 20(2):79–83. <https://doi.org/10.1107/s0021889887087090>
- Tian J, Peng D, Wu X et al (2017) Electrodeposition of Ag nanoparticles on conductive polyaniline/cellulose aerogels with increased synergistic effect for energy storage. *Carbohydr Polym* 156:19–25. <https://doi.org/10.1016/j.carbpol.2016.09.005>
- Trindade ECA, Antônio RV, Brandes R et al (2020) Carbon fiber-embedded bacterial cellulose/polyaniline nanocomposite with tailored for microbial fuel cells electrode. *J Appl Polym Sci*. <https://doi.org/10.1002/app.49036>
- Visakh PM, Thomas S, Oksman K, Mathew AP (2012) Effect of cellulose nanofibers isolated from bamboo pulp residue on vulcanized natural rubber. *BioResources* 7:2156–2168
- Wang Y, Jing X (2008) Formation of polyaniline nanofibers: A morphological study. *J Phys Chem B* 112:1157–1162. <https://doi.org/10.1021/jp076112v>
- Wang J, Wang X, Tang H et al (2018) Ultrasensitive electrochemical detection of tumor cells based on multiple layer CdS quantum dots-functionalized polystyrene microspheres and graphene oxide – polyaniline composite. *Biosens Bioelectron* 100:1–7. <https://doi.org/10.1016/j.bios.2017.07.077>
- Wang D, Bai T, Cheng W et al (2019a) Surface Modification of bamboo fibers to enhance the interfacial adhesion of epoxy resin-based composites prepared by resin transfer molding. *Polymers (basel)* 11:2107. <https://doi.org/10.3390/polym11122107>
- Wang T, Liu X, Han D et al (2019b) In-situ synthesis of BiVO₄ QDs/cellulose fibers composite for photocatalytic application. *Int J*

- Hydrogen Energy 44:31969–31978. <https://doi.org/10.1016/j.ijhydene.2019.10.096>
- Woigk W, Fuentes CA, Rion J et al (2019) Fabrication of flax fibre-reinforced cellulose propionate thermoplastic composites. *Compos Sci Technol* 183:107791. <https://doi.org/10.1016/j.compscitech.2019.107791>
- Xu G, Wang L, Liu J, Wu J (2013) FTIR and XPS analysis of the changes in bamboo chemical structure decayed by white-rot and brown-rot fungi. *Appl Surf Sci* 280:799–805. <https://doi.org/10.1016/j.apsusc.2013.05.065>
- Xu QF, Liang CF, Chen JH et al (2020) Rapid bamboo invasion (expansion) and its effects on biodiversity and soil processes +. *Glob Ecol Conserv* 21:e00787. <https://doi.org/10.1016/j.gecco.2019.e00787>
- Yakubu MT, Bukoye BB (2009) Abortifacient potentials of the aqueous extract of *Bambusa vulgaris* leaves in pregnant Dutch rabbits. *Contraception* 80:308–313. <https://doi.org/10.1016/j.contraception.2009.03.003>
- Yang H, Yan R, Chen H et al (2007) Characteristics of hemicellulose, cellulose and lignin pyrolysis. *Fuel* 86:1781–1788. <https://doi.org/10.1016/j.fuel.2006.12.013>
- Yang C, Chen C, Pan Y et al (2015) Flexible highly specific capacitance aerogel electrodes based on cellulose nanofibers, carbon nanotubes and polyaniline. *Electrochim Acta* 182:264–271. <https://doi.org/10.1016/j.electacta.2015.09.096>
- Yang S, Sun L, An X, Qian X (2020) Construction of flexible electrodes based on ternary polypyrrole@cobalt oxyhydroxide/cellulose fiber composite for supercapacitor. *Carbohydr Polym* 229:115455. <https://doi.org/10.1016/j.carbpol.2019.115455>
- Zhang X, Wang F, Keer LM (2015) Influence of surface modification on the microstructure and thermo-mechanical properties of bamboo fibers. *Materials (basel)* 8:6597–6608. <https://doi.org/10.3390/ma8105327>
- Zhao H, Kwak JH, Wang Y et al (2007) Interactions between cellulose and N-methylmorpholine-N-oxide. *Carbohydr Polym* 67:97–103. <https://doi.org/10.1016/j.carbpol.2006.04.019>
- Zheng W, Lv R, Na B et al (2017) Nanocellulose-mediated hybrid polyaniline electrodes for high performance flexible supercapacitors. *J Mater Chem A* 5:12969–12976. <https://doi.org/10.1039/C7TA01990D>
- Zhou L-P, Liu B, Li Z-Y (2004) Study of charge transport in highly conducting polymers based on a random resistor network. *Phys Lett A* 333:322–327. <https://doi.org/10.1016/j.physleta.2004.10.029>
- Zhou Z, Yang Y, Han Y et al (2017) In situ doping enables the multifunctionalization of templately synthesized polyaniline@cellulose nanocomposites. *Carbohydr Polym* 177:241–248. <https://doi.org/10.1016/j.carbpol.2017.08.136>

Publisher's Note Springer Nature remains neutral with regard to jurisdictional claims in published maps and institutional affiliations.